



OPEN ACCESS

EDITED BY

Kaijie Xu,
University of Alberta, Canada

REVIEWED BY

Fang Song,
Jilin University, China
Yufeng Pan,
Huazhong University of Science and
Technology, China
Min Guo,
Shaoxing University, China

*CORRESPONDENCE

Bo Sun,
✉ sunbo@tyut.edu.cn

RECEIVED 01 February 2025

ACCEPTED 20 February 2025

PUBLISHED 12 March 2025

CITATION

Sun B, Li Y, Gao Z and Zhang M (2025)
Quartz-enhanced photoacoustic
spectroscopy for SF₆ gas matrix based on a
T-shaped quartz tuning fork.
Front. Phys. 13:1569734.
doi: 10.3389/fphy.2025.1569734

COPYRIGHT

© 2025 Sun, Li, Gao and Zhang. This is an
open-access article distributed under the
terms of the [Creative Commons Attribution
License \(CC BY\)](https://creativecommons.org/licenses/by/4.0/). The use, distribution or
reproduction in other forums is permitted,
provided the original author(s) and the
copyright owner(s) are credited and that the
original publication in this journal is cited, in
accordance with accepted academic practice.
No use, distribution or reproduction is
permitted which does not comply with
these terms.

Quartz-enhanced photoacoustic spectroscopy for SF₆ gas matrix based on a T-shaped quartz tuning fork

Bo Sun^{1,2*}, Yue Li¹, Zhijian Gao¹ and Mingjiang Zhang^{1,2}

¹College of Physics and Optoelectronics, Taiyuan University of Technology, Taiyuan, China, ²Shanxi Key Laboratory of Precision Measurement Physics, Taiyuan University of Technology, Taiyuan, China

This paper presents the design and fabrication of a T-shaped quartz tuning fork (QTF) for quartz-enhanced photoacoustic spectroscopy (QEPAS) gas sensing systems, specifically targeting the detection of decomposition products in sulfur hexafluoride (SF₆). Through theoretical analysis and simulations, the geometrical parameters of the T-shaped QTF were optimized to achieve a low resonant frequency of 12.46 kHz and a quality factor of 4,587 in SF₆ gas matrix. The optimized system demonstrated a minimum detection limit (MDL) of 1 ppm for C₂H₂ in SF₆ matrix, with a normalized noise equivalent absorption (NNEA) coefficient of $2.037 \times 10^{-8} \text{ cm}^{-1} \text{ W}/\sqrt{\text{Hz}}$. This study successfully validates the effectiveness of the T-shaped QTF for sensitive gas detection in SF₆ matrix, providing a promising technical solution for online monitoring of decomposition products and fault diagnosis in SF₆-insulated equipment.

KEYWORDS

QEPAS, SF₆ decompositions, quartz tuning fork, trace gas detection, micro-resonator

1 Introduction

With the accelerated global transition to green and low-carbon energy, the demand for clean electricity is rapidly increasing. To accommodate the challenges posed by the integration of high proportions of renewable energy sources into power grids, grid systems are expanding in scale and complexity. This necessitates enhanced intelligence, automation, and resilience in power grids [1, 2]. To safeguard industrial security and socio-economic stability, it is essential to leverage smart grids and advanced sensing technologies for intelligent monitoring, fault prediction, and rapid recovery. Gas-insulated switchgear (GIS), utilizing SF₆ gas for its exceptional insulation and arc-quenching capabilities, has emerged as a key element of modern high-voltage power systems, superseding conventional oil-insulated equipment [3]. Fault prediction and diagnosis in GIS are of paramount importance for the reliable operation of power systems. The development of a fault detection system tailored for GIS equipment is needed.

SF₆ is widely used as an ideal insulating medium due to its properties as a colorless, odorless, non-toxic, and non-flammable gas with a density of 146 g/mol. Its insulation strength is 2–3 times greater than that of air, and it possesses high dielectric strength, remaining relatively stable at room temperature [4–6]. However, operational issues within GIS, such as arcing, partial discharges, or excessive temperatures, can cause SF₆ to decompose into lower fluorides like SF₄, SF₂, and S₂F₁₀ [7]. These lower fluorides can react with trace amounts of oxygen and water vapor present in the equipment under

discharge and high-temperature conditions, generating corrosive byproducts including SO_2 , SOF_2 , SO_2F_2 , SOF_4 , H_2S , HF , and CO . These decomposition products may deposit on the surfaces of insulating materials, thereby increasing the risk of corrosion and dielectric breakdown in metallic components, which can lead to equipment malfunction. Moreover, some decomposition products, including SO_2 , SOF_2 , HF , and CO , are toxic, presenting health concerns [8, 9].

In GIS equipment, different types of faults can generate various species and concentrations of SF_6 decomposition products. By analyzing these decomposition products in conjunction with historical operational data, it is possible to infer the potential fault types and their severity [10]. Currently, SF_6 decomposition product detection primarily employs four methods: gas chromatography, electrochemical sensors, gas detection tubes, and Fourier-transform infrared spectroscopy [11–18]. Gas chromatography effectively separates complex gas mixtures with high precision and stability; however, its sample preparation process is cumbersome, time-consuming, and costly, making it unsuitable for rapid on-site testing [11, 12]. Electrochemical sensors offer a quick response to changes in gas concentration, making them suitable for real-time monitoring and field applications, but they have a limited lifespan and higher maintenance costs [12–14]. Gas detection tubes are easy to operate but provide lower accuracy and are susceptible to human error [15, 16]. Fourier-transform infrared spectroscopy, based on laser spectroscopic techniques, mitigates uncertainties associated with chemical reactions; nonetheless, its detection sensitivity remains limited and is prone to interference from environmental noise [14, 17, 18].

Photoacoustic spectroscopy (PAS) based on absorption spectroscopy technology [19], analyzes trace gases by detecting the acoustic signals released when these gases absorb laser energy at specific wavelengths, thereby obtaining the spectral information of the gas within its characteristic absorption wavelength range and facilitating the analysis of gas compositions and concentration measurement [20–25]. As an emerging laser spectroscopic technique, QEPAS has developed rapidly since it was first introduced by Professor Frank's team at Rice University in 2002 [26–29]. In QEPAS, a low-cost, compact QTF serves as the acoustic detector. The modulated laser beam passes unobstructed through the two prongs of the tuning fork, and the resultant photoacoustic signal, which is proportional to both the laser power and the target gas concentration, causes the prongs to vibrate synchronously in opposite directions (antisymmetric bending mode). The piezoelectric effect of quartz allows the bending of the QTF prongs to generate piezoelectric charges, which are collected by the metal coating on the surface of the fork and transmitted via electrodes connected to the QTF, enabling the inversion of the target gas concentration. One significant advantage of QEPAS technology is that it operates without optical detectors, thus exhibiting characteristics such as wavelength independence and a direct correlation between detection sensitivity and laser power. Moreover, QEPAS utilizes the QTF to replace traditional broadband microphones used in PAS, leveraging the QTF's small size, low-cost, high-quality factor [30–35].

The standard commercial QTFs used in QEPAS technology exhibit several limitations. First, the 0.3 mm prong spacing of standard QTFs in QEPAS requires precise optical beam alignment,

as contact between the excitation light and prongs causes significant interference. This limitation complicates the application of longer-wavelength infrared, high-power LED, and THz laser sources. Second, the modulation frequency in photoacoustic spectroscopy is determined by the resonance frequency of the QTF. Standard QTF with 32.7 kHz resonance frequency restricts the efficient detection of gases with slow relaxation, resulting in low electroacoustic conversion. Additionally, in SF_6 gas matrix, standard commercial QTFs face significant challenges. The SF_6 molecule has a high density and mass, resulting in a relatively slow diffusion rate. This means that at higher frequencies, the vibrational response of the QTF is notably restricted, leading to ineffective detection of low concentrations of SF_6 decomposition products [36, 37]. Under these conditions, the responsiveness of the QTF to heavier molecules, such as SF_6 and its byproducts, declines further, reducing detection sensitivity. Moreover, the high resonance frequency of the QTF hinders the capture of thermal acoustic signals from gas molecules, particularly in applications requiring high sensitivity, leading to signal loss. To address these issues in the promotion of QEPAS technology, it is crucial to design a new type of customized QTF with a lower resonance frequency and wider prong spacing. However, increasing the prong spacing will lead to an upward trend in resonance frequency, and changes in this parameter may affect the quality factor of the tuning fork. Therefore, the development of high-performance custom tuning forks requires sound theoretical guidance to ensure their effective application in SF_6 gas matrix.

This paper presents our recent advancements in the design, fabrication, and application of a customized quartz tuning fork (QTF) for SF_6 decomposition product detection via quartz-enhanced photoacoustic spectroscopy (QEPAS). Specifically, we designed and fabricated a novel T-shaped QTF, characterized by its wider prong spacing, lower resonance frequency, and maintained high-quality factor—features crucial for efficient QEPAS sensing in SF_6 matrix. To validate the performance of this custom QTF in a QEPAS sensor, a C_2H_2 gas sensor was constructed using a distributed feedback (DFB) laser with a center wavelength of 1,532 nm as the excitation source, and its performance metrics were systematically evaluated. This approach not only demonstrates the capability of the T-shaped QTF to overcome the common limitations of standard QTFs in SF_6 matrix, but it also presents a practical pathway for high-sensitivity and high-selectivity detection of SF_6 decomposition products, thereby enabling improved fault diagnosis in GIS equipment.

2 Customized QTF design and performance

The SF_6 molecule possesses a large mass and density, which reduces molecular diffusion rates and significantly impacts the vibrational characteristics of QTFs. Commercially available standard QTF exhibit a quality (Q)-factor of 12,741 in N_2 , but the Q-factor drops to 3,757 in SF_6 , rendering their sensing capabilities ineffective [37]. To achieve efficient QEPAS detection in SF_6 matrix, the geometrical and electrical parameters of the QTF can be tailored to better match the requirements of the QEPAS technique. In fact, the resonant frequency and quality factor of the QTF are critical parameters influencing the performance of QEPAS sensors.

Starting analysis from the resonant frequency (f_0) of the QTF, for effective demodulation of the photoacoustic signal, f_0 must be equal to the modulation frequency (f_a) of the excitation source. Furthermore, f_a and the radiative lifetime (τ) of the gas molecules must satisfy the condition $f_a \tau \ll 1$ to ensure efficient excitation of the photoacoustic signal [33]. It is necessary to lower the resonant frequency of the QTF to match the slower molecular relaxation rates of various SF_6 decomposition products and to avoid signal loss at high frequencies due to the diffusion limitations of SF_6 molecules. Considering the Q-factor of the QTF, which represents the ratio of the total energy stored by the fork to the energy dissipated per oscillation cycle, a higher Q value indicates that the tuning fork can amplify the signal to a greater extent based on resonance. However, in high-purity SF_6 gas matrix, pursuing an excessively high Q-factor is not desirable due to the damping effect of the SF_6 gas on the QTF. An overly high Q-factor can lead to a sluggish response of the QTF to the photoacoustic signals generated by the decomposition products, hindering the rapid capture of signals originating from these products. It is crucial to optimize the Q-factor of the QTF so that it can effectively amplify the signal of decomposition products while also responding quickly to changes in the decomposition product signal. Consequently, the QTF design for SF_6 gas matrix must simultaneously address the reduction of resonant frequency while maintaining an appropriate Q-factor and accounting for the effects of gas damping, ultimately achieving sensitive and efficient detection of SF_6 and its decomposition products.

According to the Euler-Bernoulli equation, the resonant frequency f_0 of a QTF is closely related to its geometrical parameters, such as prong length L , width T , and the gap S between two prongs [38, 39]:

$$f_0 = \frac{1.194^2 \pi T S}{8 \sqrt{12} L^2} \sqrt{\frac{E}{\rho}}$$

Here, ρ and E represent the density and Young's modulus of the material used to fabricate the QTF, respectively. For quartz, a material renowned for its excellent temperature stability of the piezoelectric coefficient, these values are $2,650 \text{ kg/m}^3$ and $0.72 \times 10^{11} \text{ N/m}^2$, respectively. Considering the influence of the spacing between the QTF prongs on the ease of optical collimation of the excitation source, to reduce the resonant frequency f_0 , the width of the prongs should be decreased while increasing their length.

Regarding the Q-factor of the QTF, this parameter reflects the energy dissipation level of the QTF prong during a single oscillation cycle. The losses can generally be categorized into intrinsic and extrinsic losses, such as losses due to friction with the surrounding gas and thermoelastic damping. These losses coexist but are not correlated with each other, and currently, there are no established theories or formulas to accurately quantify them. Among these various losses, the loss due to gas friction is typically much greater than the sum of the other losses. Therefore, in our theoretical analysis, we can approximate by only considering these types of loss. The empirical formula related to this gas friction loss is given by [36]:

$$Q = \frac{4\rho w t^2 f_0}{3\mu t + \frac{3}{4}t\sqrt{4\pi\rho_0\mu f_0}}$$

where μ is the gas viscosity, ρ_0 is the gas pressure, and t is the thickness of the QTF. Substituting the expression for f_0 into the above

equation, it becomes evident that to achieve a high Q-factor, the width of the prongs should be increased, along with an increase in the QTF's resonant frequency f_0 . However, when the frequency is less than 10 kHz, it is not guaranteed that $Q > 10,000$ at atmospheric pressure. Clearly, for conventional QTF geometries, a high Q-factor and a low resonant frequency cannot be simultaneously achieved. Therefore, a compromise must be made in selecting appropriate parameters while increasing the spacing between the prongs.

Based on the preceding analysis, a T-shaped QTF was designed. A detailed schematic is shown in Figure 1, T_1 , T_2 , L_1 , and L_2 represent the widths and lengths of the top and bottom sections of the T-shaped QTF prongs, respectively. By the aforementioned expressions for the QTF's resonant frequency and Q-factor, we can initially determine the range of values for each geometrical parameter. Further refinement of these parameters requires modeling the QTF by COMSOL software and conducting simulation calculations. Then, the QTF's prong thickness, t , the total prong length, L , and the width of the prong T_1 , were set to 0.25 mm, 9.4 mm, and 2 mm, respectively, based on the parameters of a previously fabricated novel wide-prong-spacing QTF [40]. Given that the electrode pattern used in the experiment extends approximately 2.4 mm from the top, L_1 was set to 2.4 mm. The electrode pattern, in this case, refers to the thin metallic film, electroplated onto the quartz surface after QTF fabrication to conduct the piezoelectric signal. A gold film was employed to maximize protection against corrosion damage to the quartz QTF caused by the highly corrosive components SO_2 , SOF_2 , SO_2F_2 , SOF_4 , and H_2S , which are often found in SF_6 decomposition products. However, despite these measures, due to the inevitable presence of H_2O molecules in GIS equipment, H_2S can still react with gold under the presence of H_2O to form Au_2S , affecting the accuracy of the output piezoelectric signal. Therefore, periodic inspection of the detection module is necessary to ensure the equipment's accuracy.

Furthermore, COMSOL simulation results indicate a positive linear relationship between the QTF's base resonant frequency and the ratio T_2/T_1 , with a 70% threshold. When T_2/T_1 is less than 70%, the QTF's resonant frequency drops below 10 kHz. However, further reduction of this ratio increases the instability of the QTF's geometrical and mechanical model, thus compromising stable oscillation of the QTF. Therefore, T_2/T_1 was set to 0.7, leading to $T_2 = 1.4 \text{ mm}$. After completing the theoretical parameter settings, a T-shaped QTF, as depicted in Figure 1 and named T-S08-QTF, were fabricated from quartz material. The electrical parameters of these QTFs were then experimentally measured. The measured frequency response curves of the T-S08-QTF in N_2 and SF_6 matrix are shown in Figure 2. By performing a Lorentzian fit to these response curves, it can be determined that the resonant frequency and Q-factor of the T-S08-QTF, as presented in Table 1. These measured values are in good agreement with the theoretical calculations and validating the theoretical model. The Q-factor of the T-S08 QTF in SF_6 is nearly 1,000 higher than that of conventional standard QTF.

3 System setup and parameter optimization

To validate the performance of the T-S08-QTF in a QEPAS system, a gas sensing system was constructed, as shown in Figure 3,

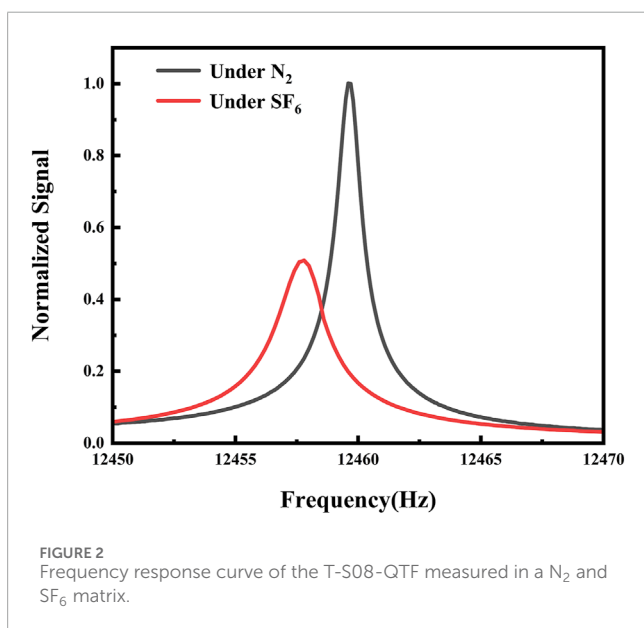
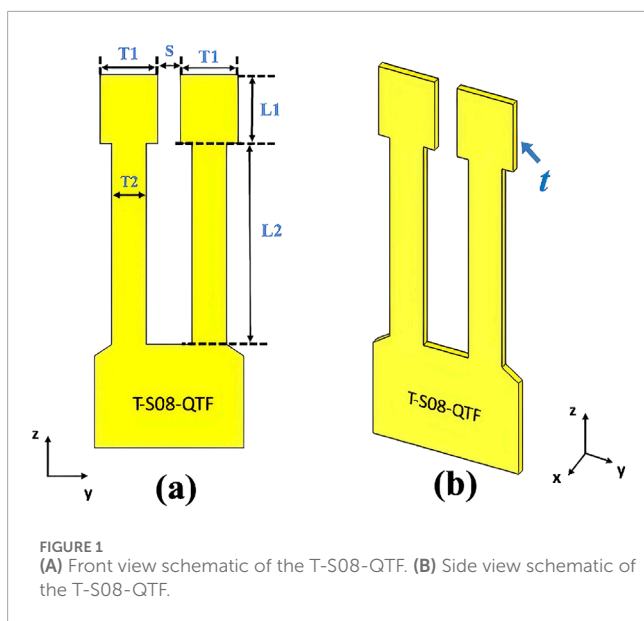
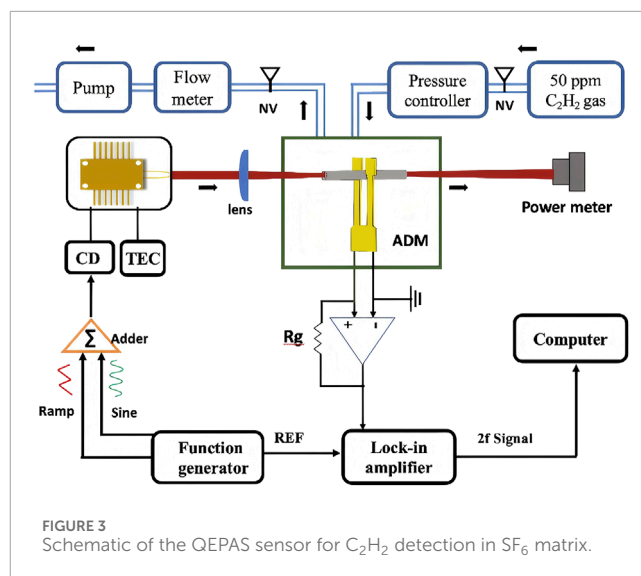


TABLE 1 Resonant frequency (f_0), Q-factor, and resistance (R) of the T-S08-QTF in N_2 and SF_6 environments.

Matrix gas	F_0 (Hz)	Q factor	R (K Ω)
N_2	12460	8160	209
SF_6	12457.6	4587	359

using acetylene (C_2H_2) as the target analyte. After consulting the HITRAN database, the C_2H_2 absorption line at 6523.88 cm^{-1} was selected as the operating wavelength for the excitation source. Consequently, a near-infrared distributed feedback (DFB) laser, packaged in a butterfly configuration, was employed here. The laser's temperature and current were controlled by a driver board. The QEPAS spectrophone consisted of the T-S08-QTF and a



miniature acoustic micro-resonator, sealed within a $\sim 100\text{ cm}^3$ stainless steel gas cell. The gas cell was equipped with 25 mm diameter calcium fluoride optical windows on either side to ensure sufficient interaction between the excitation source and the gas within the cell. The transmittance of the windows exceeded 95% for the excitation source. The laser light was delivered to the gas cell through a fiber with a focusing lens, passing non-contact through the optical micro-resonator and the T-S08-QTF with its large prong spacing. A power meter was placed behind the gas cell to measure the laser power in real-time. The gas cell ports were equipped with inlet and outlet interfaces, connected to a gas line that included a diaphragm pump, needle valve, pressure controller, and flow meter, to control and monitor the pressure and flow rate within the gas line. Based on the selected C_2H_2 absorption line, the DFB laser's temperature was adjusted to 13.8°C , matching the laser's center wavelength with the target absorption line. A complete C_2H_2 absorption spectrum could be obtained by applying a scanning current. To reduce background noise and enhance the signal-to-noise ratio, a $2f$ wavelength modulation photoacoustic detection method was employed in this QEPAS sensor. Wavelength modulation of the DFB laser was achieved by applying a modulated current, with the modulation frequency set to half of the T-S08-QTF's resonant frequency. The piezoelectric current generated by the T-S08-QTF was converted into a voltage signal by a transimpedance amplifier with a feedback resistor of $10\text{ M}\Omega$ and then connected to the signal input of a lock-in amplifier (Stanford Research System, SR830). The synchronous signal input of the lock-in amplifier was synchronized with the modulation signal output of a function generator, enabling the demodulation of the voltage signal at twice the modulation frequency and the acquisition of the second harmonic signal, which is related to the target gas concentration. The lock-in amplifier's integration time was set to 300 ms, the filter slope was set to 12 dB/octave, and the corresponding detection bandwidth was 0.833 Hz.

In QEPAS gas sensing systems, the spectrophone is a core component, consisting of a QTF and a micro-resonator. The micro-resonator typically comprises a pair of thin-walled stainless steel

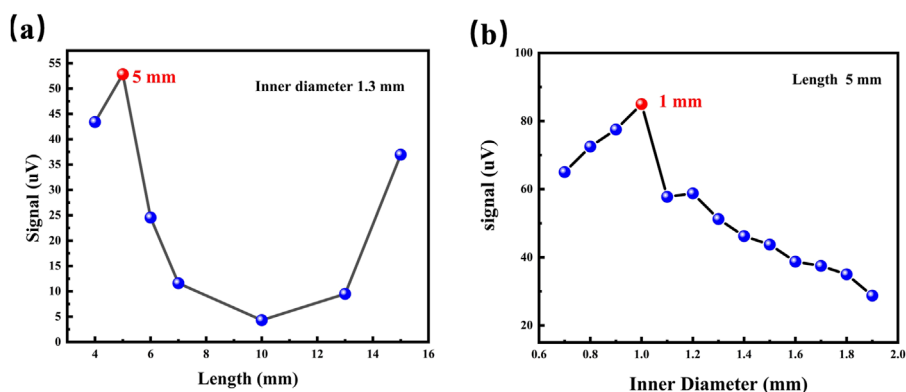


FIGURE 4 (A) Micro-Resonator length optimization results; (B) Micro-Resonator inner diameter optimization results.

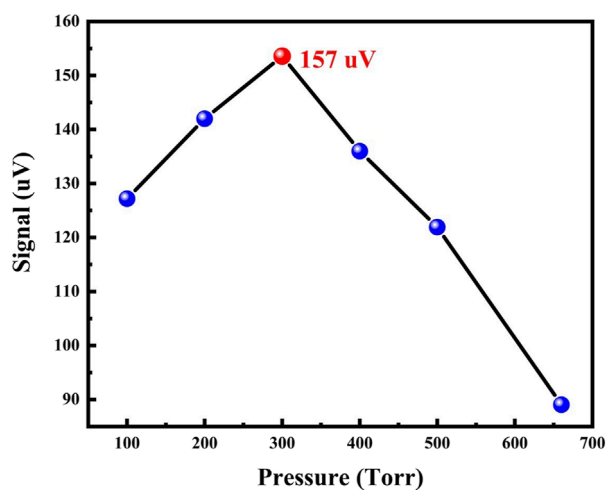


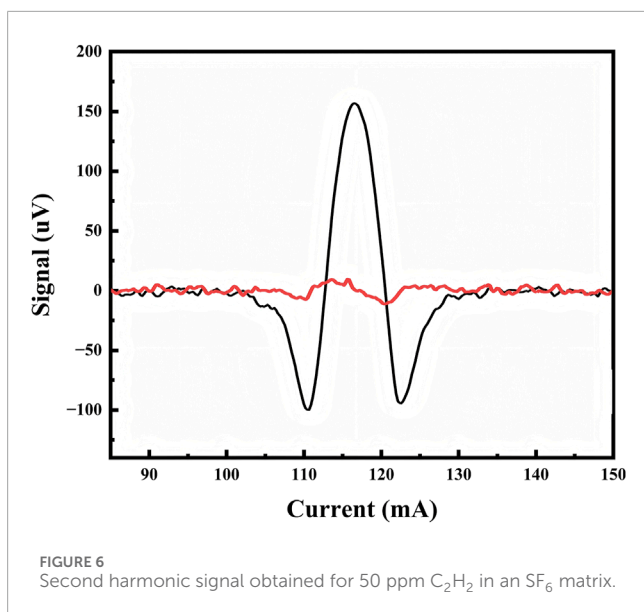
FIGURE 5 Optimization results for the operating pressure of the QEPAS system.

tubes with small inner diameters. The two tubes are symmetrically positioned on either side of the QTF along the optical path, vertically aligned such that the center of each tube is positioned 1.5 mm from the tips of the QTF prongs, with each tube leaving a small gap with the outer sides of the QTF prongs. As an acoustic micro-resonator, the resonant tubes can enable the photoacoustic signal to resonate within the micro-resonator and form a standing wave, thus enhancing the photoacoustic signal intensity. To achieve the optimal signal collection and amplification effect of the micro-resonator, its geometrical dimensions need to be optimized. Since the prongs gap distance of the T-S08-QTF is 0.8 mm, the inner diameter of the micro-resonator should be no less than 0.8 mm to allow a relatively large optical spot size to pass through the QTF without contact. In this experiment, resonant cavities with a 1.3 mm inner diameter were first fabricated from thin stainless steel. The 50 ppm C_2H_2 signal was then collected while the micro-resonator length was adjusted from 4 mm to 15 mm. This optimization experiment was conducted at standard atmospheric pressure and

room temperature about 24°C, the resulting C_2H_2 peak signal data are shown in Figure 4A. A maximum signal of 53 μV was obtained at a resonator length of 5 mm. With the resonator length fixed at 5 mm, the resonant resonator's inner diameter was then further optimized by adjusting it from 0.7 mm to 1.9 mm. The resulting 50 ppm C_2H_2 peak signal data are shown in Figure 4B. A maximum signal of 87 μV was obtained at an inner diameter of 1 mm. Therefore, the optimal resonator length and inner diameter dimensions for the micro-resonator were determined to be 5 mm and 1 mm, respectively. The modulation depth used in the system during the above experiments was a previously optimized value of 13 mA.

In QEPAS systems, optimization of the operating pressure is necessary. Initially, as the gas chamber pressure gradually increases from an extremely low pressure, the gas molecule density increases, leading to a stronger interaction between laser and matter, and consequently, an increase in the photoacoustic signal. On the other hand, as the ambient pressure continues to rise, the gas molecule density further increases, and the frequency of collisions with the QTF increases. This significantly increases the gas damping effect, which constrains the free vibration of the QTF, increases vibrational energy loss, and thus weakens the vibration performance, resulting in a decrease in the photoacoustic signal. Therefore, due to the combined effect of these two opposing factors, finding an optimal pressure balance point is necessary to obtain the best photoacoustic signal. Data measurements were taken every 100 Torr, starting from 100 Torr. The measurement analyte was the 50 ppm C_2H_2 signal in an SF_6 matrix. This process allowed us to analyze the impact of different pressures on sensor performance and to identify the optimal operating conditions. The experimental results, shown in Figure 5, indicate that the sensitivity of the QEPAS sensor increases significantly with increasing pressure, reaching a peak when the pressure reaches 300 Torr. However, as the pressure continues to increase beyond 300 Torr, the C_2H_2 signal begins to decrease.

After completing the aforementioned parameter optimization experiments, the detection sensitivity of the C_2H_2 sensor based on the T-S08-QTF was experimentally determined. The 2f-QEPAS



signal of the acetylene gas and the noise background signal were measured by operating the system at 300 torr, with the gas chamber filled with a 50 ppm C₂H₂/SF₆ mixture, as shown in Figure 6. The results indicate that the signal amplitude obtained was 157 μV. The 1σ noise level, determined from the background signal with high-purity SF₆, was 3 μV. Based on this, the MDL of the system for C₂H₂ gas under atmospheric conditions was determined to be 1 ppm. Considering the system's detection bandwidth of 0.833 Hz and the excitation light power of 21 mW, the NNEA coefficient of the system was calculated to be $2.037 \times 10^{-8} \text{ cm}^{-1} \text{ W}/\sqrt{\text{Hz}}$.

4 Summary

This paper theoretically analyzes the influence of QTF geometric parameters on its resonant frequency and Q-factor, considering the high density and large molecular mass characteristics of SF₆ gas. Based on this analysis, a T-shaped quartz tuning fork (T-S08-QTF) with a lower resonant frequency (~12.46 kHz) and a larger prong spacing (0.8 mm) was designed and fabricated. The experimentally measured Q-factors of the T-S08-QTF in N₂ and SF₆ environments were 8,160 and 4,587, respectively, which are in good agreement with theoretical predictions. A QEPAS gas sensing system based on the T-S08-QTF was constructed, and system parameters were optimized using C₂H₂ as the target gas. Through experiments, the optimal micro-resonator length and inner diameter of the acoustic micro-resonator were determined to be 5 mm and 1 mm, respectively. The optimized operating pressure was 300 Torr. The experimental results show that with 50 ppm C₂H₂/SF₆ gas mixture, the MDL of the system for acetylene was 1 ppm, and the NNEA coefficient was $2.037 \times 10^{-8} \text{ cm}^{-1} \text{ W}/\sqrt{\text{Hz}}$. This study successfully designed and fabricated a novel T-shaped QTF suitable for gas detection in SF₆ matrix and demonstrated its effectiveness in a QEPAS sensor system. The optimized QEPAS sensor exhibited good sensitivity and a low detection limit,

offering a promising approach for detecting SF₆ decomposition products in gas-insulated equipment. Future work will explore the T-S08-QTF's performance in detecting specific decomposition products (SO₂, SOF₂, HF, CO), its long-term stability, and anti-interference capabilities. Further system optimization, including advanced data processing, will enhance detection accuracy and reliability.

Data availability statement

The datasets presented in this article are not readily available because The dataset can be accessed through a collaborative agreement. Requests to access the datasets should be directed to sunbo@tyut.edu.cn.

Author contributions

BS: Conceptualization, Data curation, Formal Analysis, Funding acquisition, Investigation, Methodology, Project administration, Resources, Software, Supervision, Validation, Visualization, Writing—original draft, Writing—review and editing. YL: Writing—review and editing. ZG: Writing—review and editing. MZ: Writing—review and editing, Funding acquisition.

Funding

The author(s) declare that financial support was received for the research, authorship, and/or publication of this article. National Key Research and Development Program of China (2023YFF0715700); Natural Science Foundation of China (U23A20375).

Conflict of interest

The authors declare that the research was conducted in the absence of any commercial or financial relationships that could be construed as a potential conflict of interest.

Generative AI statement

The author(s) declare that no Generative AI was used in the creation of this manuscript.

Publisher's note

All claims expressed in this article are solely those of the authors and do not necessarily represent those of their affiliated organizations, or those of the publisher, the editors and the reviewers. Any product that may be evaluated in this article, or claim that may be made by its manufacturer, is not guaranteed or endorsed by the publisher.

References

- Medina C, Ríos MAC, González G. Transmission grids to foster high penetration of large-scale variable renewable energy sources—A review of challenges, problems, and solutions. *Int J Renew Energ Res (Ijrer)* (2022) 12(1):146–69. doi:10.20508/ijrer.v12i1.12738.g8400
- Hassan Q, Hsu C-Y, Mounich K, Algburi S, Jaszczur M, Telba AA, et al. Enhancing smart grid integrated renewable distributed generation capacities: implications for sustainable energy transformation. *Sustainable Energ Tech Assessments* (2024) 66:103793. doi:10.1016/j.seta.2024.103793
- Yang X, Chen B, He Y, Zhu C, Zhou X, Liang Y, et al. Ppb-level SO₂ photoacoustic sensor for SF₆ decomposition analysis utilizing a high-power UV laser with a power normalization method. *Sensors* (2024) 24(24):7911. doi:10.3390/s24247911
- Jong EC, Macek PV, Perera IE, Luxbacher KD, McNair HM. An ultra-trace analysis technique for SF₆ using gas chromatography with negative ion chemical ionization mass spectrometry. *J Chromatogr Sci* (2015) 53(6):854–9. doi:10.1093/chromsci/bmu154
- Yin X, Dong L, Wu H, Gao M, Zhang L, Zhang X, et al. Compact QEPAS humidity sensor in SF₆ buffer gas for high-voltage gas power systems. *Photoacoustics* (2022) 25:100319. doi:10.1016/j.pacs.2021.100319
- Williams SRO, Moate PJ, Hannah MC, Ribaux BE, Wales WJ, Eckard RJ. Background matters for the SF₆ tracer method for estimating enteric methane emissions from dairy cows: a critical evaluation of the SF₆ procedure. *Anim Feed Sci Technol* (2011) 170(3–4):265–76. doi:10.1016/j.anifeeds.2011.08.013
- Dervos CT, Vassiliou P. Sulfur hexafluoride (SF₆): global environmental effects and toxic byproduct formation. *J Air & Waste Manage Assoc* (2000) 50(1):137–41. doi:10.1080/10473289.2000.10463996
- Rhrissi I, Bouhrouche A, Arba Y, Moubah R. AlC₃ monolayer: highly responsive and selective gas sensing material for SF₆ decomposed gases (SOF₂, SO₂F₂ and SO₂). *Colloids Surf A: Physicochemical Eng Aspects* (2024) 700:134724. doi:10.1016/j.colsurfa.2024.134724
- Mahdi AS, Abdul-Malek Z, Arshad RN. SF₆ decomposed component analysis for partial discharge diagnosis in GIS: a review. *IEEE Access* (2022) 10:27270–88. doi:10.1109/access.2022.3156926
- Chen B, Li H, Zhao X, Gao M, Cheng K, Shao X, et al. Trace photoacoustic SO₂ gas sensor in SF₆ utilizing a 266 nm UV laser and an acousto-optic power stabilizer. *Opt Express* (2023) 31(4):6974–81. doi:10.1364/oe.483240
- Kórh O, Rikker T, Molnár G, Mahara BM, Torkos K, Borossay J. Study of decomposition of sulphur hexafluoride by gas chromatography/mass spectrometry. *Rapid Commun Mass Spectrom* (1997) 11(15):1643–8. doi:10.1002/(sici)1097-0231(19971015)11:15<1643::aid-rcm14>3.3.co;2-3
- Liu C-H, Palanisamy S, Chen S-M, Wu P-S, Yao L, Lou B-S. Mechanism of formation of SF₆ decomposition gas products and its identification by GC-MS and electrochemical methods: a mini review. *Int J Electrochem Sci* (2015) 10(5):4223–31. doi:10.1016/j.s1452-3981(23)06617-8
- Thirumalraj B, Palanisamy S, Chen S-M, Wu P-S, Yao L, Lou B-S. Electrochemical sensing of SF₆ decomposition products based on a screen printed carbon electrode. *Int J Electrochem Sci* (2015) 10(4):3098–105. doi:10.1016/s1452-3981(23)06522-7
- Dong M, Zhang C, Ren M, Albarracín R, Ye R. Electrochemical and infrared absorption spectroscopy detection of SF₆ decomposition products. *Sensors* (2017) 17(11):2627. doi:10.3390/s17112627
- Suehiro J, Zhou G, Hara M. Detection of partial discharge in SF₆ gas using a carbon nanotube-based gas sensor. *Sensors Actuators B: Chem* (2005) 105(2):164–9. doi:10.1016/j.snb.2004.05.050
- Zhang X, Zhang Y, Tang J, Cui Z, Li Y, Zhou H, et al. Optical technology for detecting the decomposition products of SF₆: a review. *Opt Eng* (2018) 57(11):110901. doi:10.1117/1.oe.57.11.110901
- Luo ZC, Han FY, Tang B, Zhang LF, Liu CY, Liang QQ, et al. Optical properties and decomposition mechanisms of SF₆ at different partial discharge determined by infrared spectroscopy. *AIP Adv* (2018) 8(6):065107. doi:10.1063/1.5030524
- Zhang X, Yan J, Zhang Y, Cheng L, Bian C, Chen X. Infrared spectrum analysis and quantitative detection of SF₆ characteristic decomposition components SO₂F₂ and SOF₂. *IEEE Trans Dielectr Electr Insul* (2022) 29(4):1316–23. doi:10.1109/tdei.2022.3183654
- Liu C, Wang G, Zhang C, Patimisco P, Cui R, Feng C, et al. End-to-end methane gas detection algorithm based on transformer and multi-layer perceptron. *Opt Express* (2024) 32(1):987. doi:10.1364/oe.511813
- Yin X, Wu H, Dong L, Li B, Ma W, Zhang L, et al. Ppb-level SO₂ photoacoustic sensors with a suppressed absorption–desorption effect by using a 7.41 μm external-cavity quantum cascade laser. *ACS Sensors* (2020) 5(2):549–56. doi:10.1021/acssensors.9b02448
- Li B, Wu H, Feng C, Wang J, Jia S, Zheng P, et al. Photoacoustic heterodyne CO sensor for rapid detection of CO impurities in hydrogen. *Anal Chem* (2023) 96(1):547–53. doi:10.1021/acs.analchem.3c04753
- Yin X, Gao M, Miao R, Zhang L, Zhang X, Liu L, et al. Near-infrared laser photoacoustic gas sensor for simultaneous detection of CO and H₂S. *Opt Express* (2021) 29(21):34258–68. doi:10.1364/oe.441698
- Li B, Feng C, Wu H, Jia S, Dong L. Photoacoustic heterodyne breath sensor for real-time measurement of human exhaled carbon monoxide. *Photoacoustics* (2022) 27:100388. doi:10.1016/j.pacs.2022.100388
- Liu X, Cui J, Feng C, Tian Q, Cui R, Zhao Y, et al. Differential photoacoustic cell-based Fourier transform photoacoustic spectroscopy for background-free gas detection [Invited]. *Chin Opt Lett* (2024) 22(10):101203. doi:10.3788/col202422.101203
- Wei Q, Li B, Zhao B, Yang P, Dong L. Photoacoustic spectroscopy for fault diagnostics in high voltage power transmission systems: a review. *Measurement* (2024) 227:114259. doi:10.1016/j.measurement.2024.114259
- Kosterev AA, Bakhirkin YA, Curl RF, Tittel FK. Quartz-enhanced photoacoustic spectroscopy. *Opt Lett* (2002) 27(21):1902–4. doi:10.1364/ol.27.001902
- Kinjalk K, Paciolla F, Sun B, Zifarelli A, Menduni G, Giglio M, et al. Highly selective and sensitive detection of volatile organic compounds using long wavelength InAs-based quantum cascade lasers through quartz-enhanced photoacoustic spectroscopy. *Appl Phys Rev* (2024) 11:021427. doi:10.1063/5.0189501
- Li B, Feng C, Wu H, Jia S, Dong L. Calibration-free mid-infrared exhaled breath sensor based on BF-QEPAS for real-time ammonia measurements at ppb level. *Sensors Actuators B: Chem* (2022) 358:131510. doi:10.1016/j.snb.2022.131510
- Wang J, Wu H, Sampaolo A, Patimisco P, Spagnolo V, Jia S, et al. Quartz-enhanced multiheterodyne resonant photoacoustic spectroscopy. *Light: Sci & Appl* (2024) 13:77. doi:10.1038/s41377-024-01425-1
- Wu H, Dong L, Zheng H, Yu Y, Ma W, Zhang L, et al. Beat frequency quartz-enhanced photoacoustic spectroscopy for fast and calibration-free continuous trace-gas monitoring. *Nat Commun* (2017) 8(1):15331. doi:10.1038/ncomms15331
- Dong L, Kosterev AA, Thomazy D, Tittel FK. QEPAS spectrophones: design, optimization, and performance. *Appl Phys B* (2010) 100:627–35. doi:10.1007/s00340-010-4072-0
- Wu G, Xing J, Gong Z, Ma J, Fan Y, Wu X, et al. Single fiber-type double cavity enhanced photoacoustic spectroscopy sensor for trace methane sensing. *J Lightwave Technol* (2024) 42(11):3393–8. doi:10.1109/jlt.2024.3353200
- Wu H, Dong L, Yin X, Sampaolo A, Patimisco P, Ma W, et al. Atmospheric CH₄ measurement near a landfill using an ICL-based QEPAS sensor with VT relaxation self-calibration. *Sensors Actuators B: Chem* (2019) 297:126753. doi:10.1016/j.snb.2019.126753
- Pan Y, Lu P, Cheng L, Li Z, Liu D, Zhao J, et al. Open-closed single-tube on-beam tuning-fork-enhanced fiber-optic photoacoustic spectroscopy. *Photoacoustics* (2024) 39:100639. doi:10.1016/j.pacs.2024.100639
- Pan Y, Fu L, Zhang J, Lu P, Liu D, Zhao J, et al. Miniaturized and highly-sensitive fiber-optic photoacoustic gas sensor based on an integrated tuning fork by mechanical processing with dual-prong differential measurement. *Photoacoustics* (2023) 34:100573. doi:10.1016/j.pacs.2023.100573
- Sun B, Zifarelli A, Wu H, Dello Russo S, Li S, Patimisco P, et al. Mid-infrared quartz-enhanced photoacoustic sensor for ppb-level CO detection in a SF₆ gas environment exploiting a T-grooved quartz tuning fork. *Anal Chem* (2020) 92(20):13922–9. doi:10.1021/acs.analchem.0c02772
- Sun B, Patimisco P, Sampaolo A, Zifarelli A, Spagnolo V, Wu H, et al. Light-induced thermoelastic sensor for ppb-level H₂S detection in a SF₆ gas matrices exploiting a mini-multi-pass cell and quartz tuning fork photodetector. *Photoacoustics* (2023) 33:100553. doi:10.1016/j.pacs.2023.100553
- Patimisco P, Sampaolo A, Dong L, Giglio M, Scamacchio G, Tittel FK, et al. Analysis of the electro-elastic properties of custom quartz tuning forks for photoacoustic gas sensing. *Sensors Actuators B: Chem* (2016) 227:539–46. doi:10.1016/j.snb.2015.12.096
- Patimisco P, Borri S, Sampaolo A, Beere HE, Ritchie DA, Vitiello MS, et al. A quartz enhanced photo-acoustic gas sensor based on a custom tuning fork and a terahertz quantum cascade laser. *Analyst* (2014) 139(9):2079–87. doi:10.1039/c3an01219k
- Dello Russo S, Giglio M, Sampaolo A, Patimisco P, Menduni G, Wu H, et al. Acoustic coupling between resonator tubes in quartz-enhanced photoacoustic spectrophones employing a large prong spacing tuning fork. *Sensors* (2019) 19(19):4109. doi:10.3390/s19194109